machines

Article

Young's Modulus and Hardness Identification of Extruded Aluminum by Scratching Damper

Chun-Nam Wong [1], Anand Vyas [2], Wai-On Wong [1,*] and Ruqi Sun [3]

[1] Department of Mechanical Engineering, The Hong Kong Polytechnic University, Hong Kong, China; chun-nam.wong@connect.polyu.hk
[2] Division of Science, Engineering and Health Studies, CPCE, The Hong Kong Polytechnic University, Hong Kong, China; anand.vyas@cpce-polyu.edu.hk
[3] School of Automobile, Chang'an University, Xi'an 710064, China; sunruqi@chd.edu.cn
* Correspondence: wai.on.wong@connect.polyu.hk

Abstract: A special vibration damper is proposed for Young's modulus and hardness identification through a scratching process on extruded aluminum. This paper presents the design and working principle of a scratching damper based on a scratching device. A non-contact electromagnetic shaker is used to generate the shaking force for test sample vibration. The required forces on the scratched material during the scratching process are generated by an adjustable compression spring. The proposed damper is designed and tested on an extruded aluminum 3004 sample for the determination of its Young's modulus and hardness, and validation is performed using the standard test instruments. The physical dimensions of the scratching tracks are measured using a microscope and utilized to compute the scratching energy factor. Load curves are obtained at different divisions of the scratching process. The loop energy during the scratching process of the tested object is measured and used for the determination of sample material properties. Furthermore, the energy conservation law, scratch energy release rate of semi-conical scratch head, and loop energy release rate are established to determine the Young's modulus and hardness of the sample. Their estimation accuracies are evaluated. The proposed method has several advantages over the traditional methods, including low cost, directness, and high repeatability. The results suggest this to be used as an alternative to the standard modulus and hardness tester.

Keywords: scratching damper; energy release rate; scratch energy conservation; extruded aluminum 3004; Brinell hardness

Citation: Wong, C.-N.; Vyas, A.; Wong, W.-O.; Sun, R. Young's Modulus and Hardness Identification of Extruded Aluminum by Scratching Damper. *Machines* **2024**, *12*, 413. https://doi.org/10.3390/machines12060413

Academic Editors: José Balthazar, Angelo Marcelo Tusset, Átila Madureira Bueno, Diego Colón and Marcus Varanis

Received: 30 April 2024
Revised: 11 June 2024
Accepted: 14 June 2024
Published: 17 June 2024

1. Introduction

In order to acquire the material property via a scratch test, different experimental processes and analytical methods have been implemented. Kamplade and Biermann [1] utilized scratch tests to analyze the grain performance while grinding thermoplastics. Corundum grains were used in two different scratch test set-ups for fundamental analysis of the material removal process. The scratching process was evaluated according to the relative material removal volumes of the scratch grooves. In addition to that, the forces occurring during the process and the required specific scratch energy were analyzed. Scratch tests using a Rockwell-C diamond cone indenter were reported by Varga et al. [2], where the test load was induced with a slip-stick mechanism. Line scars were produced on the specimen after scratching. Scratch topographies and average profiles for increasing the scratch load were studied, and their cross-sections were analyzed. Moreover, studies on numerical simulations of the scratch process have also been reported using smooth particle hydrodynamics [3].

The energy required to create a unit fracture surface was computed by Akono and Ulm [4] using an energetic contour-independent J-integral. The energy release rate was linked to stress intensity factors in mode I and II via the Griffith–Irwin equation [5]. Their equation on mode I failure coincided with our plain strain analysis. Finite element meshing was performed on crack tip. Using the fracture criterion, the forces and tool geometry were linked to the plane strain fracture toughness [6]. Cross-sectional investigations were carried out and analyzed. Moreover, it is reported [7] that the elastic modulus and hardness of silicon carbide particle-reinforced aluminum matrix composites, SiCp/Al, were determined through the indentation test by loading onto an Al matrix and SiC particles generating three material phases during the deformation process. More complicated effects were reflected in the applied load scratch depth (P-h) curves. A relative accurate result is obtained from a single-phase material in our test. In ultrasonic vibration-assisted machining tests, precision or ultra-precision machining was combined with micro-scale (1–15 μm) and high-frequency (16–40 kHz) tool or workpiece vibration. In this paper, the authors use the test dimension at the millimeter scale up to several mm and lower frequency around 10 Hz.

A scratch test on glass ceramics [8] has shown that crack propagation increases linearly with the material removal volume. Wakeel and Hubler [9] introduced heterogeneity into the micro-scratch test fracture. A similar formulation for the J-integral is utilized in our scratch energy derivation. Akono and Ulm [10] established the fracture scaling relations for scratch tests of axisymmetric shape of a scratch indenter in which the equivalent force is composed of the scratch force and indentation force. Kamplade and Biermann [1] examined the material removal of unreinforced, thermoplastic polymers by scratch tests to analyze the grain engagement. A helical scratch groove was produced using a single grain. Also, the indentation force and specific scratch energy were measured at a specific wheel speed. In this damper test, multiple averaged tracks were formed instead of a more irregular single groove. Smooth finishing on the sample surface was achieved. Measurements of scratch dimensions, such as scratch depth, contact length, and removal volume, were enhanced.

To determine the Young's modulus of aluminum, ultimate stress, Young's modulus, and the ultimate strains of normal and high strength were considered for aluminum 6063-T5 and 6061-T6 at elevated temperatures [11]. Their ratios were related systematically to the temperature ratio using the Ramberg and Osgood equation [12]. Janeczek and Fydrych [13] compared the effect of the shape of a tool on the joint to obtain the values of the friction stir welding parameters. A tensile strength test of aluminum alloy 3004 was conducted. The influence of the tool pin shape on the contact intensity was studied. The hardness of the forged precipitation-hardened aluminum alloy EN AW-2618A for different aging times and temperatures was obtained by Rockenhäuser et al. [14]. The Brinell hardness number was computed by DIN EN 6506-1 [15].

In this investigation, Young's modulus and the hardness of aluminum 3004 are estimated using scratching theory. In a traditional scratch test, a static load is applied to obtain the fracture surface when the test is conducted one time in a certain direction and is not repeatable. There might be unstable indenter movement along the path, depending on the material–indenter interaction. In our case, cyclic vibration load was used instead, generating a repeatable load-path loop. As a result, a stable smooth fracture surface was created. This generated refined sub-layer scratching within the test material, facilitating in-depth property analysis. Moreover, in the computation of the scratch damping ratio, the load profile at scratch path, test speed, and scratching force at indenter tip could be accurately measured by vibration sensors. Furthermore, the indenter was changeable from a round-head shape for damping motion to a pin-head shape for significant scratching motion.

2. Design and Working Principle of Scratching Damper

An innovative damper was modified from the existing EMSD-RCFD DVA developed by Sun, Wong, and Cheng [16]. A divisional scratching test was conducted through scratch damping, where the required load could be adjusted by dial knot divisions. The test-rig schematic of the scratching damper is illustrated in Figure 1a. A non-contact electromagnetic exciter was mounted on top of the mounting frame that provided the excitation force without introducing any additional stiffness to the dynamic system, as shown in Figure 1b. The exciter coil was fixed on the mounting frame, while permanent magnets were fixed on the magnet stringer rob, which can be regarded as part of the system mass. The mass, stiffness, and natural frequency of the damper system were M = 6.87 kg, K = 20.961 N/mm, and ft = 9 Hz respectively.

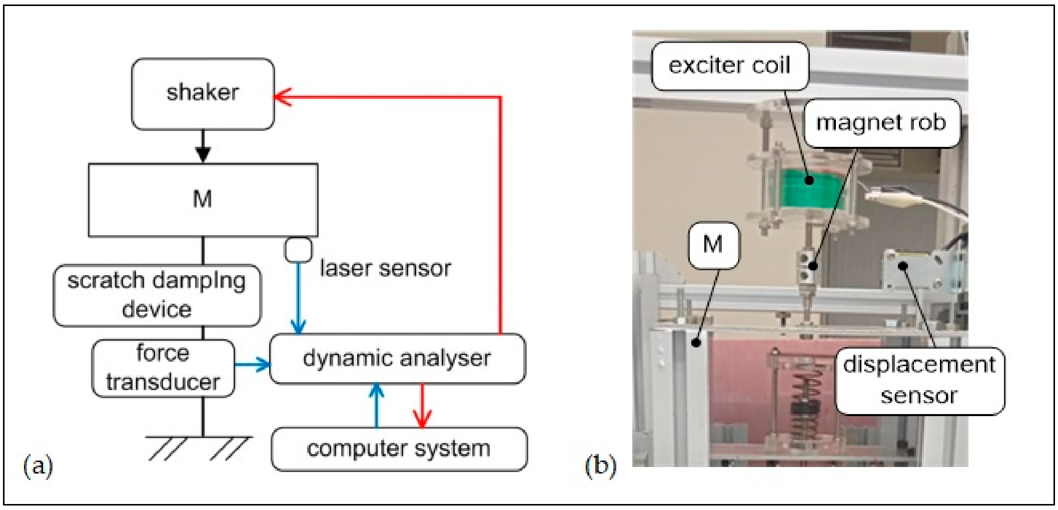

Figure 1. (**a**) Equipment schematic of scratching damper; (**b**) electromagnetic exciter and its mounting to system mass. The blue and red arrows show the input and output signals to the dynamic analyser, respectively.

The linear guide was composed of four rotation bearings on each side face, and the smooth glassy surface for bearing motion allowed for a reduction in the parasitic damping of the damper system. To measure the damper force, a force sensor was fastened to the damper rob, which was grounded to a steel table (Figure 2a). A laser sensor was used to measure the absolute displacement of the system's mass. A nylon tube, with a pre-compressed spring inside, was fixed onto the tuning mechanism of the scratching device to provide a rough linear guide for the mass vibration. The data acquisition and signal generation were conducted with the B&K PULSE 7767 system (Figure 1a). The driving signal to the exciter was amplified by the B&K 2712 power amplifier before being sent to the non-contact exciter. The device was installed in the middle part of the system.

Under the principle of scratch energy conservation, divisional scratching energy was computed by the energy equation within the same interval test:

$$U^{ji} = \wp_j^i + \Psi^{ji} \tag{1}$$

where U^{ji} is j divisional total energy of scratching motion at the ith interval, Ψ^{ji} is j divisional energy of the damping motion, $\wp_j^i = F_v^{ji} \cdot v_j^i$ is j divisional scratching energy, F_v^{ji} is j divisional scratching energy factor, and v_j^i is j divisional material removal volume. Applying the energetic contour-independent J-integral [4,9], the scratch energy release rate, which is the energy required to create a unit scratching surface, is

$$\wp = \frac{1}{p}\int_S \left(\Psi n_x - \tau_x \frac{\partial U_x}{\partial x}\right) dS \tag{2}$$

where $\Psi = \frac{\kappa}{2E}\sigma_{xx}^2$ is the free energy density with $\kappa = 1 - \nu^2$, ν is Poisson's ratio, $\frac{\partial U_x}{\partial x}$ is the displacement gradient, p is the scratch head perimeter, and $\tau_x = \sigma_{xx} n_x$ is the surface traction. ds is the differential line element and dS is the surface element, related as

$$ds = \sqrt{1 + \cot\theta^2},\ dS = r d\phi ds \tag{3}$$

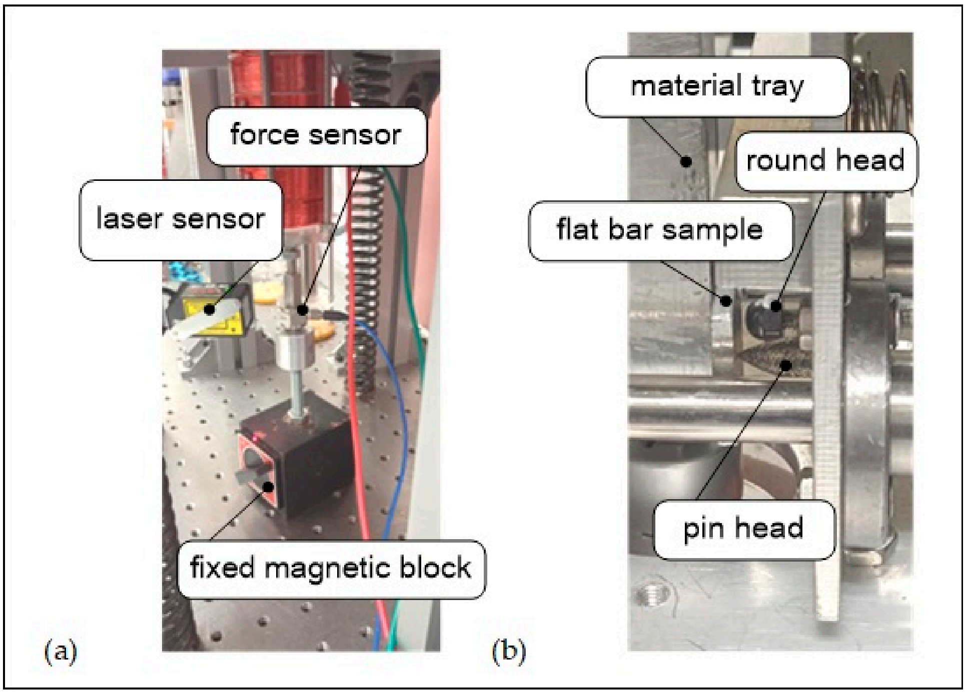

Figure 2. (**a**) Force transducer assembly of damper rob and magnetic block of scratching damper; (**b**) assembly components of scratching device in scratching damper.

For tangential track generation from the scratch head, the Airy stress function was established as [10]

$$\Gamma(x,z) = -ax\left(z^3 - \frac{3}{4}zd^2\right) + bz^2 \tag{4}$$

where a and b are constants. Its symmetric stress tensors were computed by

$$\sigma_{zz} = \frac{\partial^2 \Gamma}{\partial z^2} = -6axz + 2b \tag{5}$$

$$\sigma_{xz} = \frac{\partial^2 \Gamma}{\partial x \partial z} = a\left(3z^2 - \frac{3}{4}d^2\right) \tag{6}$$

$$\sigma_{zz} = \frac{\partial^2 \Gamma}{\partial x^2} = 0 \tag{7}$$

The displacement gradient at the scratch head–material interface was determined by the potential function:

$$\Theta = -\frac{a}{2}\left[-\frac{x^4 + z^4}{2} + 3(xz)^2\right] + 2bxz \tag{8}$$

which satisfies $\Theta_{,zz} = 0$, $\Theta_{,xz} = \sigma_{xx}$. Afterwards, the displacement gradient is calculated by:

$$\frac{\partial U_x}{\partial x} = \frac{1}{E}\left[-(1+v)\frac{\partial^2 \Gamma}{\partial x^2} + \kappa\frac{\partial^2 \Theta}{\partial z \partial x}\right] = -6axz + b = \frac{\kappa}{E}\sigma_{xx} \tag{9}$$

Substituting this to Equation (2), one can obtain

$$\wp = \frac{1}{p}\int_S -\frac{\kappa}{2E}\sigma_{xx}^2 n_x dS = \frac{\kappa}{2pE}\int_A \sigma_{xx}^2 dA' \tag{10}$$

where E is Young's modulus and p and A are the scratch head perimeter and projected contact area, respectively. On the other hand, the scratch force is given by:

$$F_t = \int_S (\sigma_{xx} n_x + \sigma_{xz} n_z) dS = \int_A \sigma_{xx} dA',\ F_n = -\int_S \sigma_{xz} n_x dS \tag{11}$$

Substituting Equations (5)–(7) into Equation (11), a and b are determined to be

$$a = -\frac{2\cot\theta F_n}{d^4},\ b = \frac{\cot\theta F_t}{2d^2} \tag{12}$$

Assuming that the stress field over the scratch head is constant, its linear stress average is related to the quadratic stress average on the projected contact area as the integral in Equation (11):

$$\int_A \sigma_{xx}^2 dA' \simeq \left(\int_A \sigma_{xx} dA'\right)^2 / \int_A dA' = \frac{F_t^2}{A} \tag{13}$$

Hence, we have the scratch energy release rate, created as:

$$\wp = \frac{1-\nu^2}{E} \frac{F_t^2}{2pA} \tag{14}$$

The semi-conical scratch head shape function, defined by Figure 3, can be generated by:

$$z = r\cot\theta \tag{15}$$

in which r is the radius of the head, $z \subset [0, d]$ is the height, and θ is the conical angle. Firstly, p projected onto the scratch direction is generated from Equation (2):

$$p = \int ds = \int_0^{d/\cot\theta} \sqrt{1+\cot\theta^2} dr = \frac{d}{\cot\theta}\sqrt{1+\cot\theta^2} = \frac{d}{\cos\theta} \tag{16}$$

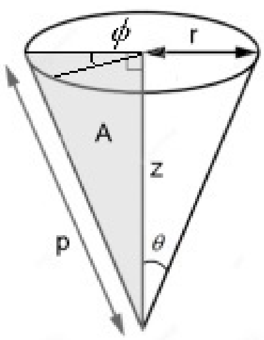

Figure 3. Dimensions of semi-conical scratch pin head.

Secondly, the scratch surface projected in the scratch direction becomes:

$$A = \int n_x dS = \int \hat{n} \cdot e_x r \sqrt{1+\cot\theta^2} d\phi dr \tag{17}$$

where $\hat{n} = \frac{\cot\theta\cos\phi}{\sqrt{1+\cot\theta^2}} e_r + \frac{1}{\sqrt{1+\cot\theta^2}} e_z$. For the semi-conical head, the cylindrical angle is $\phi \subset [0, \pi/2]$. Therefore, A can be computed using the cylindrical co-ordinate as:

$$A = \int_0^{d/\cot\theta} \int_0^{\pi/2} \cot\theta(\cos\phi r) d\phi dr = \frac{\cot\theta}{2}\left[\sin\phi|_0^{\pi/2}\right]\left[r^2\Big|_0^{d/\cot\theta}\right] = \frac{d^2\tan\theta}{2} \tag{18}$$

Substituting Equations (16) and (18) into Equation (14), one obtains the unique $\wp$ for semi-conical pin head:

$$\wp = \frac{1-\nu^2}{E}\frac{F_t^2}{d^3 \sin\theta} \tag{19}$$

3. Results and Discussion

3.1. Young's Modulus of Extruded Aluminum Flat Bar

Upon the scratch test of the extruded aluminum 3004, a flat bar sample, of the size 15(L) × 10(W) × 4(T) in mm, as shown in Figure 2b, was prepared. Special machining was not required. And the preparation was simple, consisting of cutting and fitting. Using the scratching damper, the following tests in two to four dial knot divisions of the compression spring were conducted to investigate its material properties (such as Young's modulus and hardness), as shown in Figure 4.

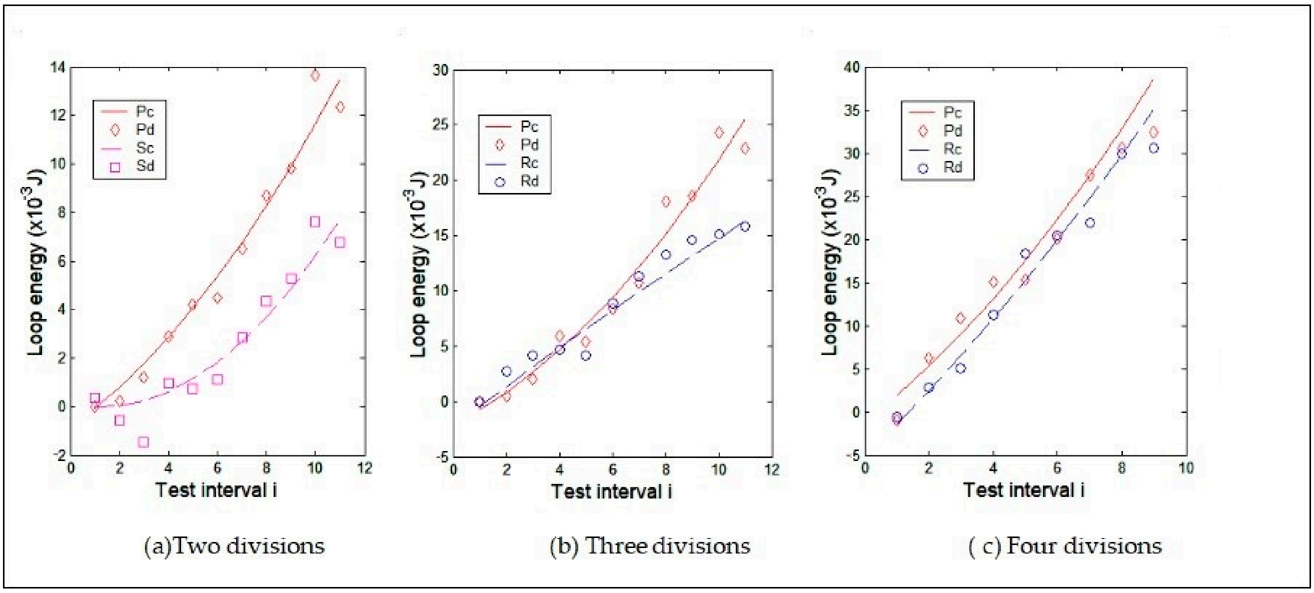

Figure 4. Divisional loop energy curves of extruded aluminum (Pc Pd curve fit and test data of U^j_{pin}, Rc Rd curve fit and test data of Ψ^j_{round}, Sc Sd curve fit and test data of $\wp_j$).

These load curves indicate that the loop energy increased consecutively with the interval load [5–8]. The loop energy is the area integration of the F_t- displacement loop measured by the force transducer and laser sensor in Figure 2a. Figure 4a complies with Akono and Ulm [10] in that the scratching energy release rate increased with the test interval in a quadratic curve [1,11]. Meanwhile, the damping energy increased with the test interval in a linear curve, as shown in Figure 4a,b. The summation of loop energy per interval with the conical pinhead is the divisional total energy, expressed as:

$$U^j_{pin} = \sum_{i=1}^{N} U^{ji}_{pin} \cdot j \cdot f_t \cdot l_t/2 \tag{20}$$

where U^{ji}_{pin} is the single-loop energy with the pin head, i is the number of the test interval, j is the dial division of the test, f_t = 9 Hz is the fixed-sine test frequency, and l_t = 48 s is the test period. It is interesting to observe that the shape of the loop is highly repeatable within the same test period, with nearly 500 cycles. Meanwhile, the summation of the loop damping energy per interval with the round head is expressed as:

$$\Psi^{j}_{round} = \sum_{i=1}^{N} \Psi^{ji}_{round} \cdot j \cdot f_t \cdot l_t/2 \tag{21}$$

where Ψ^{ji}_{round} is the single-loop energy with the round head. According to Equation (1), the scratching energy per interval with j divisions is

$$\wp_j = U^{j}_{pin} - \Psi^{j}_{round} \tag{22}$$

The divisional scratching energy release rate is

$$\wp_j = \sum_{i=1}^{i=N} \frac{\wp^{i}_{j}}{N \cdot j} \tag{23}$$

Meanwhile, according to Equation (14), the divisional Young's modulus stands as:

$$E_j = \frac{1-v^2}{\wp_j} \times \frac{Feq_j^2}{2p_jA_j} \tag{24}$$

with notations in j divisions. The results from two to four divisions are given in Table 1. In general, their values decreased slightly with the scratch performance. Two divisions were the best at 29.5%. Thus, through the two-divisional test, the ith interval E^{i}_{2} was generated. We observed that it increased to a maximum, then dropped steadily to a stable value. Hence, from the Nth data, the ultimate Young's modulus was obtained as $E^{N}_{2} = 54.6$ GPa.

Table 1. Extruded aluminum material property comparison from scratching test.

Data\Dial Division	**2**	**3**	**4**
Normal force F^{j}_{n} (N)	0.16	0.24	0.32
Total energy U^{j} (J)	35.2	56.5	78.8
Damping motion energy Ψ^{j} (J)	24.8	47.8	70.3
Scratch energy $\wp_j$ (J)	10.4	8.69	8.51
Scratch performance $\wp_j/U^{j}$ (%)	29.5	15.4	10.8
Young's modulus E_j (GPa)	54.6	56.2	56.8
Hardness H^{B}_{j}	73.4	76.1	77.5
Scratch depth D_j (mm)	0.193	0.176	0.180
Scratch length L^{j} (mm)	3.38	3.10	2.92
Scratch volume V^{j} (mm^3)	0.183	0.160	0.141
Scratch energy factor F^{j}_{v} (GJ/m^3)	56.8	54.5	60.2

A tensile test is utilized to validate the Young's modulus of extruded aluminum. Five samples of nominal size—57.4(L) × 19.1(W) × 2.76(T) in mm—were cut perpendicular to their extruded directions. The tensile testing machine was set to pull typical samples until a fracture was exhibited (Figure 5a). A stress–elongation curve was generated by the machine as shown in Figure 5b.

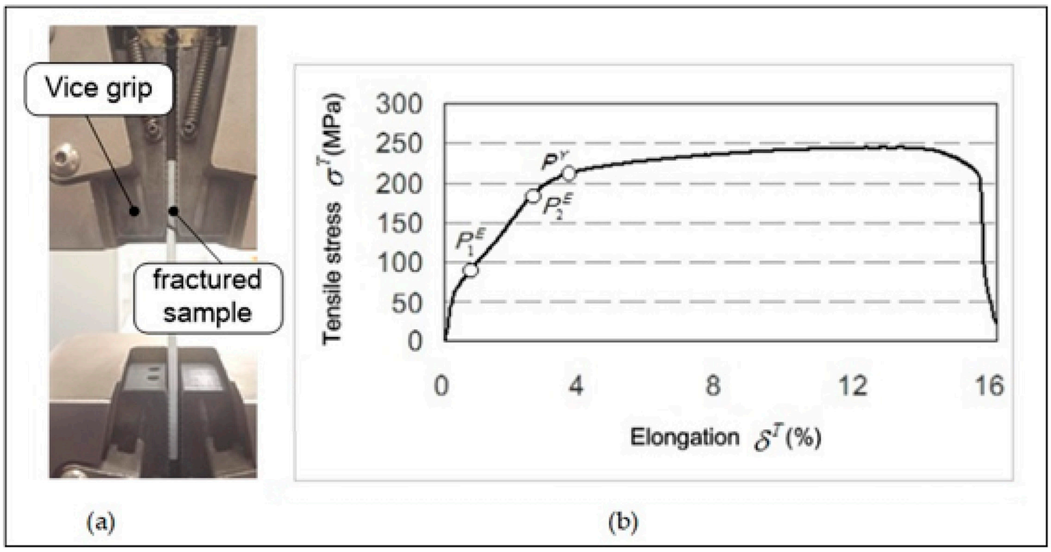

Figure 5. (**a**) Fracture of aluminum sample during tensile test; (**b**) stress–elongation curve generated by tensile testing machine ($P_1^E(92.9, 0.78)$, $P_2^E(179, 2.42)$, $P^Y(210, 3.5)$).

According to the analysis of Su and Young [11], Young's modulus of extruded aluminum varies linearly in initial stage of this curve. Changes in tensile stress $\Delta\sigma$ and elongation $\Delta\delta$ at separate positions $P_1^E = (92.9, 0.78)$, $P_2^E = (179, 2.42)$ of the elastic region were computed. The slope of the curve was used to calculate the Young's modulus of this sample as:

$$E^T = \frac{\Delta\sigma}{\Delta\delta} = \frac{\sigma_2^T - \sigma_1^T}{\delta_2^T - \delta_1^T} \times \frac{L}{WT} \tag{25}$$

The generated value was $E^T = 57.2$ GPa, +4.55% larger than E_2^N. As reported by Janeczek and Fydrych [13], a positive deviation arose at the excessive fracture, and material removal occurred at a high scratch performance using the pin head tool. This tended to underestimate E_2^i at a slightly lower tensile strength. $\Delta\delta$ was 1.64%, which is close to the 3% of Tamadon [17].

For extruded aluminum, its normalized dependence of the actual Young's modulus ratio $E_r = E_a/E_o$ on the actual density ratio $\rho_r = \rho_a/\rho_o$ for the flat bar sample [18] can be formed from the following exponential equation [12,19,20]:

$$E_r = w\rho_r^u \tag{26}$$

where w = 0.974 is fitting constant, u = 1.862 is fitting exponent as given by Kovacik and Simancik [18], and $E_o = 68$ GPa for pure aluminum 3004 [13]. Using a digital weight test, $\rho_a = 2475\ \mathrm{kg/m^3}$. From the wrought aluminum alloy data of WA-3004 [19], $\rho_o = 2720\ \mathrm{kg/m^3}$. Thus, the extruded density $\rho_r = 2475/2720 = 0.91$ was found to be 0.91. Substituting ρ_r and E_o into this equation, $E_a = 55.6$ GPa was determined for the extruded sample. This only deviated from the measured E^T by -2.9%. In the tool pin shape comparison [13,21–23], Young's modulus of the conical pin was 70.8 GPa, 24% higher than the 43.6 GPa of the thread pin. This trend reveals that the conical pin tended to provide more intense contact [13,24,25]. The semi-conical pin fell within the range providing medium-intensity contact. Janeczek and Fydrych [13] reported the tensile stress of aluminum alloy 3004 to be in the range of 175–198 MPa, with elongation of 10–16%. These are close to our test results, within a 10% deviation [26,27].

3.2. Hardness Estimation and Brinell Test

The hardness of the extruded aluminum was computed as follows. The divisional contact stiffness is given as

$$\frac{dP_j^i}{dH_j^i} = \frac{\beta}{\sqrt{\pi}} \times \frac{Feq_j^{i\,2}}{p_j^i \wp_j^i \sqrt{A_j^i}} \tag{27}$$

where β is the scratch head correction factor. From this equation, P_j is computed by its integration. Zheng et al. [7] showed that the test load increased with the square of the scratch depth. This complies with our data showing that P_j varied quadratically with A_j. Initially, it gradually increased, and then increased more rapidly afterwards. Meanwhile, divisional tensile stress was computed as:

$$H_j^i = \frac{P_j^i}{A_j^i} \tag{28}$$

Their tensile stresses were quadratic curve-fitted to the Brinell hardness number as illustrated by Ali et al [28]. Using four divisional tests, H_4^i increased to a stable peak at H_4^N. According to definition of the $P_j - A_j$ curve, hardness was evaluated at the peak load. Thus, tensile stress was calculated using its Nth interval as $H_4^N = P_4^N / A_4^N = 215$ MPa. This value was within the 40–270 MPa range of the aluminum 3000 series [29]. As a common metal in the industrial market, a wrought aluminum flat bar is prepared by the extrusion plastic-forming process [30,31]. Its yield strength was raised by the strain rate and temperature during this extrusion process [30,32,33]. As recorded by the Aluminum Association, the yield strength increased from 50 MPa to 350 MPa as the temperature decreased from 450 °C to 25 °C. Despite the decrease in Young's modulus due to the decrease in extruded density, the hardness was relatively higher throughout this process. Thus, the tensile stress at 0.2% yield point P^Y of Figure 5b, $\sigma^Y = 210$ MPa, was relatively high at the 74th percentile [27]. Meanwhile, the hardness was 75 using the Brinell tester, as in Equation (30). From the analysis of Ali [28], the hardness–tensile stress quadratic curve was modified as:

$$H_j^N = 0.14 H_j^{B^2} - 0.97 H_j^B + 206 \tag{29}$$

in which unit of H_j^N is in MPa. Substituting H_4^N into this equation, its Brinell hardness number was estimated as $H_4^B = 77.5$. Using load data from two and three divisions, their hardnesses are listed in Table 1. As stated by Tamadon [17], the hardness of AA-1100 varied from the conical pin of 140 MPa to the thread pin of 200 MPa at the yield point, which was 8% lower than H_4^N.

For existing standard tests, hardness can be measured through the Brinell hardness tester. Considering the tester in Figure 6a, an indenting load of 100 kgf was exerted on the surface of the extruded Al flat bar through a hardened steel ball 1/16 inch in diameter.

Multiple tests were carried out using the same three size samples, each with four indentations. The Brinell hardness number was used to compare the actual hardnesses. The diameter of the resulting permanent impression in a typical measured sample was 594.12 µm, as shown in Figure 6b. According to DIN EN 6506-1 [15], the Brinell hardness number was computed as

$$B_h = 2P_b / \left(\pi D_s \left(D_s - \sqrt{D_s^2 - d_I^2} \right) \right) = 75.0 \tag{30}$$

where $P_b = 100$ kgf is the load on the indenting tool, $D_s = 1.59$ mm is the diameter of the steel ball, and $d_I = 1.19$ mm is the measured diameter at the rim of indentation. This value fell into the range of 50–140, as measured by Rockenhäuser [14] and Ali [28]. Compared with H_4^5, the percentage difference was −3.37%. Negative deviation arose at the estimation of higher P_j under higher F_n^j. Due to the lower scratch performance, A_j became relatively lower. Thus, B_h tended to be slightly overestimated.

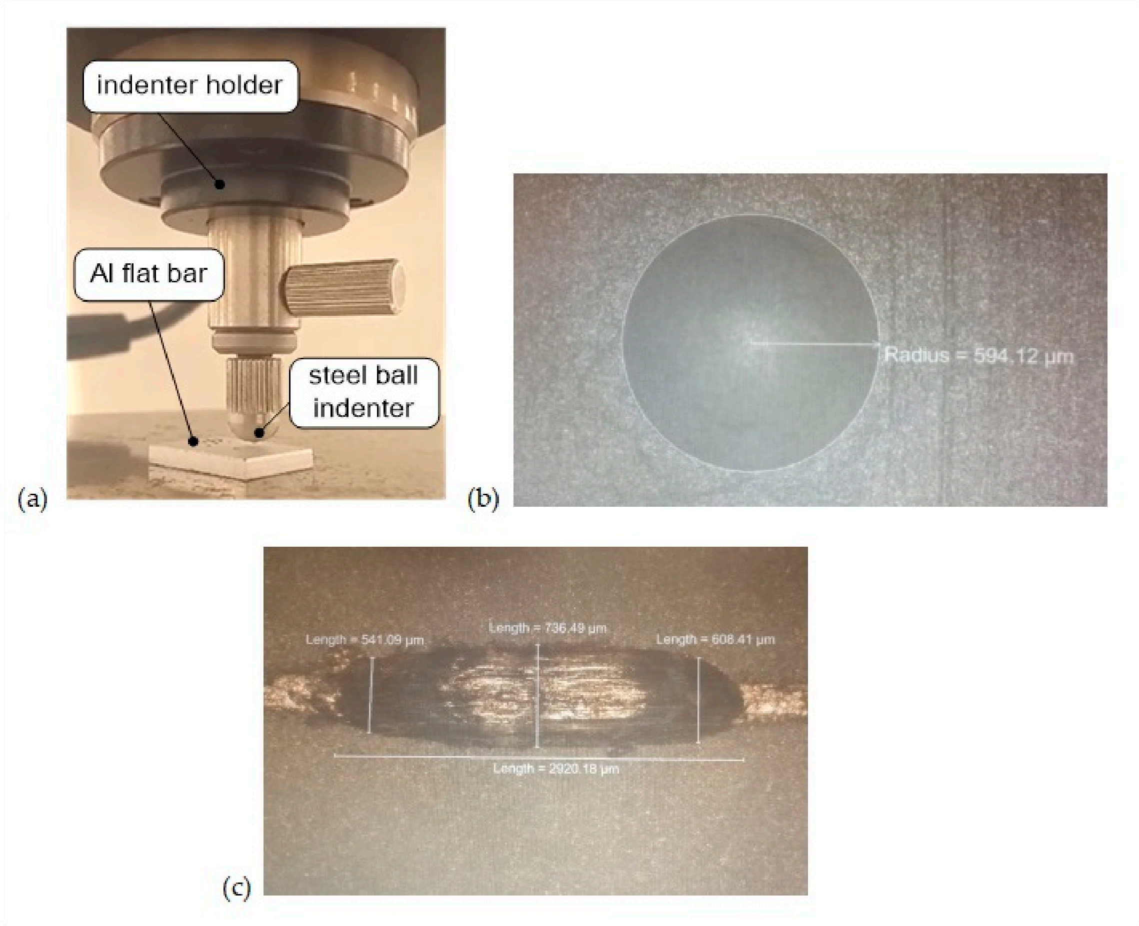

Figure 6. (**a**) Hardness tester using steel ball indenter; (**b**) microscopic measurement of steel ball indentation; (**c**) scratching track of extruded aluminum 3004.

3.3. Dimension Inspection and Performance Evaluation

In order to check the physical depth $d = D_j$ of the scratching track, a laser sensor was used to measure the depth of each track on the divisional samples. Moreover, a microscope is used to determine the physical dimensions L^j, V^j of the scratching track (Figure 6c), which were smooth and measurable. The measured data are given in Table 1 and were used to compute the material removal volume v. The scratching energy factor at j division, F_v, was computed by Equation (1), as listed in Table 1. It was stable around 56.8 GJ/m^3. From Table 1, it can be observed that U^j increased linearly with j. Simultaneously, Ψ^j increased with j at a higher linear rate. As a result, $\wp_j$ decreased with j, but was saturated at the four divisions test. The overall scratching performance $\wp_j / U^j$, decreased with j. This is in agreement with the slightly increasing trend seen in E_j and H_j estimations. On the other hand, F_v^j fluctuated around a constant value and was independent of the performance. Hence, it was independent of i or j and was in agreement with the energy conservation principle in Equation (1).

4. Conclusions

In this paper, a scratching damper is developed based on a scratching device. A cyclic vibration load is applied by the damper, creating a highly repeatable load-path loop. A smooth fracture surface was obtained, which was measurable at the microscopic scale. A round head indenter was used to provide a pure damping motion, while a pin head indenter was used to produce significant scratching motion. The scratching energy release rate was generated using free energy density and the displacement gradient of the semi-conical pin head. For comparison, the Young's modulus, E_2^N, was slightly underestimated as E^T due to a fracture and material removal upon scratching. Using a weight test, the extruded ρ_r was correctly calculated by the normalized dependence equation. For the hardness number, B_h was slightly less than the H_4^N caused by the lower scratching performance. F_v^j was found to be stable, agreeing with the energy conservation principle. The results discussed here further the study of innovative methods and the development of devices and approaches to determine material properties.

Author Contributions: Conceptualization, C.-N.W. and W.-O.W.; methodology, C.-N.W. and A.V.; software, C.-N.W.; validation, C.-N.W., W.-O.W. and A.V.; formal analysis, C.-N.W.; investigation, C.-N.W.; resources, W.-O.W. and R.S.; data curation, C.-N.W. and A.V.; writing—original draft preparation, C.-N.W.; writing—review and editing, A.V. and W.-O.W.; visualization, C.-N.W. and A.V.; supervision, W.-O.W.; project administration, W.-O.W. All authors have read and agreed to the published version of the manuscript.

Funding: This research received no external funding.

Data Availability Statement: Research data may be shared upon request.

Acknowledgments: The authors would like to thank The Hong Kong Polytechnic University for the laboratory support of the experiments in this research.

Conflicts of Interest: The authors declare no conflicts of interest.

References

1. Kamplade, K.; Biermann, D. Examination of the Material Removal of unreinforced, thermoplastic Polymers by Scratch Tests. *Prod. Eng.* **2019**, *13*, 713–719. [CrossRef]
2. Varga, M.; Leroch, S.; Rojacz, H.; Ripoll, M.R. Study of wear mechanisms at high temperature scratch testing. *Wear* **2017**, *388–389*, 112–118. [CrossRef]
3. Li, H.; Zhang, X.; Yang, X. Numerical study of liquid sloshing using smoothed particle hydrodynamics with adaptive spatial resolution. *Eng. Anal. Bound. Elem.* **2024**, *159*, 272–287. [CrossRef]
4. Akono, A.; Ulm, F. An improved technique for characterizing the fracture toughness crack growth. *Wear* **2014**, *313*, 117–124. [CrossRef]
5. Torabi, A.R.; Shahbazian, B. Notch tip plastic zone determination by extending Irwin's model. *Theor. Appl. Fract. Mech.* **2020**, *108*, 102643. [CrossRef]
6. Souza, J.M.; Yoshimura, H.N.; Peres, F.M.; Schön, C.G. Effect of sample pre-cracking method and notch geometry in plane strain fracture toughness tests as applied to a PMMA resin. *Polym. Test.* **2012**, *31*, 834–840. [CrossRef]
7. Zheng, W.; Wang, Y.; Zhou, M.; Wang, Q.; Ling, L. Material deformation and removal mechanism of SiCp/Al composites in ultrasonic vibration assisted scratch test. *Ceram. Int.* **2018**, *44*, 15133–15144. [CrossRef]
8. Qiu, Z.; Liu, C.; Wang, H.; Yang, X.; Fang, F.; Tang, J. Crack propagation and the material removal mechanism of glass–ceramics by the scratch test. *Mechnical Behav. Biomed. Mater.* **2016**, *64*, 75–85. [CrossRef]
9. Al Wakeel, S.; Hubler, M.H. Introducing heterogeneity into the micro-scratch test fracture toughness relation for brittle particle composites. *Exp. Mech.* **2018**, *58*, 1237–1247. [CrossRef]
10. Akono, A.; Ulm, F. Fracture scaling relations for scratch tests of axisymmetric shape. *Mech. Phys. Solids* **2012**, *60*, 379–390. [CrossRef]
11. Su, M.; Young, B. Material properties of normal and high strength aluminium alloys at elevated temperatures. *Thin-Walled Struct.* **2019**, *137*, 463–471. [CrossRef]
12. Ramberg, W.; Osgood, W.R. Description of Stress–Strain Curves by Three Parameters. NACA Tech. Note 902, 1943. Available online: https://ntrs.nasa.gov/citations/19930081614 (accessed on 10 June 2024).
13. Janeczek, A.; Fydrych, D. The Influence of Tool Shape and Process Parameters on the Mechanical Properties of AW-3004 Aluminium Alloy Friction Stir Welded Joints. *Materials* **2021**, *14*, 3244. [CrossRef] [PubMed]
14. Rockenhäuser, C.; Hartrott, P.; Skrotzki, B. Brinell-Hardness data (HBW 2.5/62.5) of aluminum alloy EN AW-2618A after different aging times and temperatures. *Data Brief* **2023**, *46*, 108830. [CrossRef] [PubMed]
15. *DIN EN ISO 6506-1:2015-02*; Metallic Materials—Brinell Hardness Test—Part 1: Test Method. Beuth Verlag GmbH: Berlin, Germany, 2015.
16. Sun, R.; Wong, W.; Cheng, L. Tunable electromagnetic shunt damper with opposing magnets configuration. *Smart Mater. Struct.* **2020**, *29*, 115034. [CrossRef]

17. Tamadon, A.; Baghestani, A.; Bajgholi, M.E. Influence of WC-based pin tool profile on microstructure and mechanical properties of AA1100 FSW welds. *Technologies* **2020**, *8*, 34. [CrossRef]
18. Kovacik, J.; Simancik, F. Aluminium foam—Modulus of elasticity and electrical conductivity according to percolation theory. *Scr. Mater.* **1998**, *39*, 239–246. [CrossRef]
19. Isichenko, M. Percolation Statistical Topography and Transport in Random Media. *Rev. Mod. Phys.* **1992**, *64*, 961. [CrossRef]
20. Kováčik, J. The tensile behaviour of porous metals made by GASAR process. *Acta Mater.* **1998**, *46*, 5413–5422. [CrossRef]
21. Su, H.; Xue, L.; Wu, C. Optimizing the tool pin with three flats in friction stir welding of aluminum alloy. *Int. J. Adv. Manuf. Technol.* **2020**, *108*, 721–733. [CrossRef]
22. Eyvazian, A.; Hamouda, A.M.; Aghajani, H. Study on the effects of tool tile angle, offset and plunge depth on friction stir welding of poly(methyl methacrylate)T-joint. *Proc. Inst. Mech. Eng. Part B J. Eng. Manuf.* **2019**, *234*, 773–787. [CrossRef]
23. Hemmouche, L.; Chicot, D.; Amrouche, A.; Iost, A.; Belouchrani, M.A.; Decoopman, X.; Louis, G.; Puchi-Cabrera, E.S. An analysis of the elastic properties of a porous aluminium oxide film by means of indentation techniques. *Mater. Sci. Eng. A* **2013**, *585*, 155–164. [CrossRef]
24. Sharmaa, N.; Siddiqueea, A.N.; Khana, Z.A. Material stirring during FSW of Al–Cu: Effect of pin profile. *Mater. Manuf. Process.* **2018**, *33*, 786–794. [CrossRef]
25. Shah, P.H.; Badheka, V.J. Friction stir welding of aluminium alloys: An overview of experimental findings—Process, variables, development and applications. *Proc. Inst. Mech. Eng. Part L J. Mater. Des. Appl.* **2017**, *233*, 1191–1226. [CrossRef]
26. Aluminum Association (AA). *Aluminum Design Manual (ADM)*; Aluminum Association (AA): Washington, DC, USA, 2015.
27. European Committee for Standardization, Eurocode 9: Design of aluminum structures—Part 1-2: Structural fire design, BS EN 1999-1-2, Brussels, 2007. Available online: https://www.phd.eng.br/wp-content/uploads/2014/11/en.1999.1.2.2007.pdf (accessed on 29 April 2024).
28. Ali, M.M.; Omran, A.N.M.; Mohamed, M.A. Prediction the correlations between hardness and tensile properties of aluminium-silicon alloys produced by various modifiers and grain refineries using regression analysis and an artificial neural network model. *Eng. Sci. Technol.* **2021**, *24*, 105–111.
29. *International Alloy Designations and Chemical Composition Limits for Wrought Aluminum and Wrought Aluminum Alloys*; The Aluminum Association: Washington, DC, USA, 2018; ISSN 2377-6692.
30. Li, Q.; Zhang, X.; Wang, L.; Qiao, J. The Effect of Extrusion and Heat Treatment on the Microstructure and Tensile Properties of 2024 Aluminum Alloy. *Materials* **2022**, *15*, 7566. [CrossRef] [PubMed]
31. Ma, Y.; Liu, C.; Miao, K. Effects of cooling rate and cryogenic temperature on the mechanical properties and deformation characteristics of an Al-Mg-Si-Fe-Cr alloy. *J. Alloys Compd.* **2023**, *947*, 169559. [CrossRef]
32. Wang, Y.; Xiong, L.; Feng, D. Investigation of the penetration performance of the radial forging process for Wrought Aluminium Alloy. *Materials* **2024**, *17*, 2065. [CrossRef]
33. Wang, Y.G.Y.; Zhao, S. Experimental investigation and optimization of the semisolid multicavity squeeze casting process for wrought aluminum alloy scroll. *Materials* **2020**, *13*, 5278. [CrossRef]